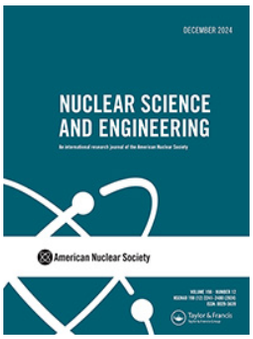

Nuclear Science and Engineering

ISSN: (Print) (Online) Journal homepage: www.tandfonline.com/journals/unse20

Experimental Investigation of Post-Dryout Heat Transfer with R-134a at High Pressures

Nikolai Rensch, Ludwig Köckert, Aurelian Florin Badea & Xu Cheng

To cite this article: Nikolai Rensch, Ludwig Köckert, Aurelian Florin Badea & Xu Cheng (16 Oct 2024): Experimental Investigation of Post-Dryout Heat Transfer with R-134a at High Pressures, Nuclear Science and Engineering, DOI: 10.1080/00295639.2024.2403890

To link to this article: https://doi.org/10.1080/00295639.2024.2403890

Published online: 16 Oct 2024.

NUCLEAR SCIENCE AND ENGINEERING

DOI: https://doi.org/10.1080/00295639.2024.2403890

Experimental Investigation of Post-Dryout Heat Transfer with R-134a at High Pressures

Nikolai Rensch,* Ludwig Köckert, Aurelian Florin Badea, and Xu Cheng

Karlsruher Institute of Technology, Institute for Applied Thermofluidics, Kaiserstraße 12, Building 07.08, 76131 Karlsruhe, Germany

Received March 26, 2024
Accepted for Publication September 4, 2024

Abstract — *An experimental study of post-dryout (PDO) heat transfer in the coolant R-134a was performed in a vertical round tube with upward flow. Experiments were conducted at high pressures from 28.4 bars up to 39.8 bars, corresponding to a reduced pressure of 0.7 to 0.98, respectively. Mass flux was varied in the interval of 300 to 1500 kg/m^2·s, and overall equilibrium vapor quality was between −1.88 and 4.89. Depending on the settings of the experimental parameters, the heat flux was varied from around 11 to 100 kW/m^2. The uniformly heated tube had an inside diameter of 10 mm and a heated length of 3000 mm.*

In total, more than 10 000 PDO data points were obtained. In the PDO region, the wall temperature distributions had similar behavior across the pressure range. At the occurrence of dryout, the wall temperature suddenly increased until it reached a peak. For higher mass flux, the wall temperature decreased after reaching the peak, followed by a second temperature increase with a lower slope. For lower mass flux, the wall temperature kept increasing after the dryout point. The temperature peak after the dryout point was smaller at higher pressure, while this effect was even stronger near the critical pressure. Likewise, the vapor quality corresponding to the first peak shifted to even lower values with increasing pressure. Furthermore, it was found that at increasing pressure and at increasing mass flux, the dryout location and the total temperature distribution shifted toward lower vapor qualities. In addition, several PDO correlations were assessed, and a new correlation for high-pressure conditions was developed and compared with the results of the existing ones.

Keywords — *Post-dryout, high pressure, R-134a, experiment, correlation.*

Note — *Some figures may be in color only in the electronic version.*

I. INTRODUCTION

Supercritical fluids will be used more often in nuclear systems of the future. During normal supercritical working conditions, the fluid is single phase and does not have the possibility to lead to a boiling crisis. However, in transient procedures, e.g., during startup or shutdown or in case of a loss-of-coolant accident, pressure may drop below the critical point. If this happens, the system will work at high subcritical pressure conditions, and that may lead to a boiling crisis with a heat flux, which is called the critical heat flux (CHF). This on the other hand may damage heating elements. CHF can distinguish between local high-quality flow and local low-quality flow. The first phenomenon is called dryout, and the second one is called departure from nucleate boiling.[1] Here, only the dryout phenomenon will be discussed.

*E-mail: Nikolai.Rensch@kit.edu

High-quality flow is usually annular flow and a vapor core with entrained droplets. Because of high velocity difference between the liquid film on the wall and the vapor core, more liquid droplets are entrained by the vapor. At the dryout point, the rate of vapor generation is high enough to lead to disappearance of the liquid film. Because of the poor heat conduction property of vapor, the wall temperature will suddenly rise.[2] Downstream from the dryout point, the heated wall is no longer wetted by a liquid film; this location is then called the post-dryout (PDO) region. The flow pattern in the PDO regime is a dispersed droplet flow.[3] During dispersed flow film boiling, the heated wall will be cooled by the following heat transfer mechanisms: vapor convection, liquid droplets impinging on the wall, and radiation. Furthermore, the heated wall will overheat the temperature of the vapor, and the vapor will transfer heat to the liquid droplets.[4] Therefore, the vapor and the liquid droplets have different temperatures. The vapor becomes superheated, and a thermal nonequilibrium state is established. The thermal nonequilibrium increases with decreasing mass flux, as confirmed by Groeneveld and Delorme.[5] Experimental studies on PDO heat transfer were performed in numerous cases, but there is still a lack of data for experiments near critical pressure.

This study expands the PDO database with R-134a coolant and complements the already existing database obtained with the KIT [Karlsruher Institute of Technology] Model Fluid Facility (KIMOF) by Köckert et al.[6] Moreover, this experimental study is of fundamental interest in the field of PDO and will be useful for possible future concepts. In addition, this study shows the strong influence of high subcritical pressure on temperature distributions. Furthermore, correlations to predict the PDO heat transfer coefficient (HTC) were assessed with the obtained data. The results and already existing data from the literature as well as the obtained data in this study were used to find out the need for further improvements of existing correlations. These were used to develop a new correlation that takes into account the influence of dispersed droplets on heat transfer in the PDO region.

II. EXPERIMENTAL FACILITY AND METHODS

II.A. Experimental Facility

The experiments were conducted at the KIMOF with its schematic illustration shown in Fig. 1 (left). The working fluid in this experimental study was the refrigerant R-134a. As shown in the scheme, a coolant pump is responsible for the circulation of the fluid. After the pump, the fluid can be preheated either by the burner or by the electric flow heater, depending on the parameters. For high mass flow, a combination of both can be used. Afterward, the mass flow will be measured by a Coriolis flowmeter, followed by the test section with temperature and pressure measurement devices, as shown in Fig. 1 (right), to be explained in the next paragraph. After the test section, two heat exchangers ensure the cooling of the fluid. The first heat exchanger is a cooling tower and operates with cooled water, and the second one works with a cooling machine. To adjust and regulate the pressure in the system, a pressurizer is used, which operates with oil on the hydraulic side. The system pressure is measured and controlled on the hydraulic side by a three-way proportional valve. During the operation of the facility, a Wago control system helps to control the entire setup. Several pressure and temperature measurement devices are installed along the facility to monitor the complete system. The data of the Wago system and four data loggers provide all relevant measurement parameters, which are further used and displayed by LabVIEW software.

II.B. Test Section

The round test tube has a total length of 3700 mm with an outer diameter of 12.7 mm and an inner diameter of 10 mm and is installed vertically. The test tube is made of Alloy 625 and can be used for temperature applications up to 1050°C. To heat up the test section, two current connectors made of copper are used, which are installed within a distance of 3000 mm. Two isolation flanges are used to avoid damage to the measurement devices and other components due to the electrical supply of the test section. The test section is heated by uniform direct current (DC) provided by a transformer. In total, 60 type-T thermocouples are alternately mounted along the outer side of the test section, and starting at thermocouples 11 and 12, every sixth thermocouple has an opposing one at the same height. The first thermocouple is mounted 655 mm above the bottom DC connector, and up to the 34th thermocouple, the longitudinal distance between each thermocouple is 60 mm. The thermocouples are mounted farther at a distance of 30 mm, and the last four thermocouples have a distance of 15 mm. The 59 and 60 thermocouples are 5 mm below the top DC connector. The thermocouples were calibrated first by the

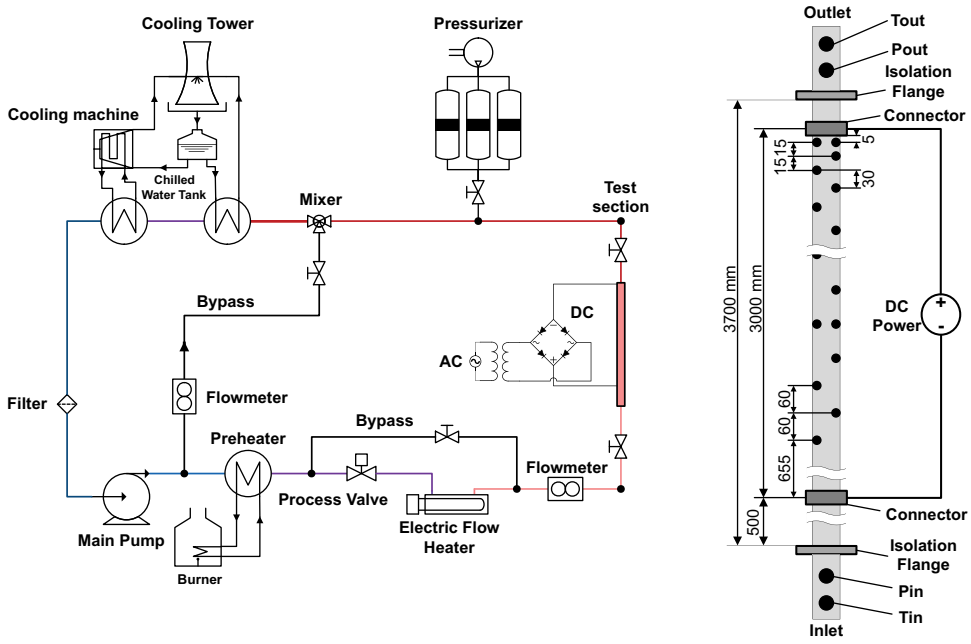

Fig. 1. On the lefthand side is the schematic setup of the KIMOF facility, and on the righthand side is the test section with the corresponding measurement devices.

manufactory and a second time before they were mounted.

The second calibration was done by using a boiler at environment pressure. The temperature and the pressure of the fluid at the inlet and outlet are measured with a mineral insulated type-T thermocouple and a pressure transmitter, respectively. The pressure is controlled by the pressurizer using the average pressure P_m of the inlet and outlet pressure sensor of the test section. To ensure a fully developed flow at the beginning of the heated section, the distance between the entrance of the tube and the bottom current connector is 500 mm. To reduce the heat loss, the test tube is surrounded by two layers of mineral wool with a total thickness of 50 mm.

II.C. Experimental Procedure and Matrix

The PDO experiments were carried out at constant pressure, inlet temperature, and mass flux as steady-state experiments. After adjusting the mentioned parameters, the heat flux was increased until the topmost thermocouple suddenly detected a strong temperature rise. After that point, the heat flux was increased in steps of either 2.5 or 5 kW/m^2, depending on the parameters. After all parameters reached a steady-state condition, a measurement was started. Each measurement took 60s, and all parameters were recorded with 2 Hz.

During one measurement, several parameters such as the inlet temperature, the mass flux, the heat flux, and the pressure must be kept within a certain range. The tolerance range of the inlet temperature was kept within $\pm$ 0.5 °C, the heat flux was kept within $\pm$ 0.5 kW/m^2, and the pressure was kept within $\pm$ 0.3bar. For the mass flux, a deviation of 2% was kept. Further increase of the heat flux shifted the onset of the dryout point in the direction of the tube entrance. This was repeated until one of the thermocouples reached the maximum outer wall temperature of around 240°C or until all thermocouples were in the PDO region. The temperature limit of 240°C was set to avoid decomposition of the refrigerant R-134a, which could change the operating conditions of the facility. Because of this maximum temperature and the limit of the heated length as well as the number of thermocouples, the heat flux was limited to a specific value, depending on the parameter combinations. The conducted experiments are shown in Table I, and the average heat flux was calculated by Eq. (1):

$$q'' = \frac{UI - Q_{loss}}{\pi L_H D_{in}} \quad , \tag{1}$$

where U is the voltage, I is the current, and the product of both is the electrical power. Q_{loss} is the heat loss calculated by Eq. (2):

TABLE I

Experimental Matrix for PDO

P_{red}	P (MPa)	x_{in}	G (kg/m^2·s)	q'' (kW/m^2)
0.7	2.84	−0.11	300,	20 to 95
0.8	3.25	[−0.15; −0.59]	600,	20 to 100
0.9	3.65	[−0.24; −0.87]	1000,	15 to 95
0.95	3.86	[−0.39; −1.23]	1500	12.5 to 85
0.98	3.98	[−0.67; −1.88]		11 to 85

$$q''_{loss} = \frac{Q_{loss}}{\pi L_H D_{out}} \quad . \tag{2}$$

The resulting power is divided by the area of the heated wall with L_H as the total heated length and D_{in} as the inner diameter of the test tube.

II.D. Test Data Reduction

The inner wall temperature was calculated by the one-dimensional, stationary Fourier heat conduction Eq. (3), with the two boundary conditions, shown in Eqs. (4) and (5):

$$\frac{d^2T}{dr^2} + \frac{1}{r}\frac{dT}{dr} + \frac{q'''}{\lambda_w} = 0 \tag{3}$$

$$-\lambda_w \left.\frac{dT}{dr}\right|_{r=r_{out}} = q''_{loss} \tag{4}$$

$$T(r = r_{out}) = T_{w,out} \quad . \tag{5}$$

The final derivation to calculate the inner wall temperature $T_{w,in}$ is shown in Eq. (6):

$$T_{w,in} = T_{w,out} + \frac{q'''}{16\lambda_w}\left(D_{out}^2 - D_{in}^2\right) + \frac{D_{out}}{2\lambda_w}\left(\frac{q'''}{4}D_{out} - q''_{loss}\right)\ln\left(\frac{D_{in}}{D_{out}}\right) \quad , \tag{6}$$

where D_{out} = outer diameter of the tube; $T_{w,out}$ = outer wall temperature; λ_w = thermal conductivity of the wall. The volumetric heat flux is calculated by Eq. (7):

$$q''' = \frac{4UI}{\pi L_H\left(D_{out}^2 - D_{in}^2\right)} \quad . \tag{7}$$

All following PDO temperature profiles show the equilibrium vapor quality, Eq. (8), versus the superheated wall temperature:

$$x_e = \frac{H - H_l}{H_v - H_l} \quad , \tag{8}$$

where H_l and H_v = enthalpies at liquid and vapor saturation, calculated at the average pressure P_m; H = enthalpy at a given axial point and can be calculated by Eq. (9):

$$H(z) = H_{in} + z\frac{Q}{\dot{m}} \quad , \tag{9}$$

where H_{in} = inlet enthalpy; Q = heat flow; $\dot{m}$ = mass flow rate. To calculate the relative length z, Eq. (10), the heated length at the point of interest $L_{H,I}$ is divided by the total heated length:

$$z = \frac{L_{H,I}}{L_H} \quad . \tag{10}$$

II.E. Measurement Uncertainties

Before the experiments were started, the devices used to measure the relevant parameters were carefully checked. The corresponding uncertainties of the test tube geometry and instrumentations are shown in Table II. An additional check was done by conducting single-phase experiments to determine the heat balance as well as vacuum experiments to determine the heat loss of the test section. For this purpose, a vacuum was set in the test section, which is why there was no convection anymore and the applied heat can be transferred only via the outer wall of the tube. The heat flux was slowly increased in small steps until the wall temperatures reached steady-state conditions. After each

TABLE II

Parameters and Their Manufacturing Uncertainties

$T_{in/out}$	$T_{w,out}$	$P_{in/out}$	m	U	I	D_{out}	s
≤1°C	≤0.98°C	0.25%	0.15%	0.03%	1.5%	0.05 mm	10%

step, a thermal equilibrium was established in which heat was transferred only because of the temperature difference between the wall of the tube and the environment. This was repeated for five different heat fluxes, and as result, the heat loss could be calculated by a polynomial function with the difference of the wall temperature and the environment temperature, which is shown in Eq. (11):

$$Q_{loss} = 0.00055\frac{W}{(^{\circ}\mathrm{C})^2}\left(T_{w,out} - T_u\right)^2 + 0.31362\frac{W}{^{\circ}\mathrm{C}}\left(T_{w,out} - T_u\right) - 0.21221W \quad . \tag{11}$$

For the heat balance experiments, the difference between the measured enthalpy and the calculated enthalpy over the test section were checked. The overall average uncertainty of the HTC was calculated to be 4.6%.

To check the reproducibility of the obtained data, experiments were repeated after around 2 months. In total, 31 PDO experiments were randomly selected and repeated. Overall, the test runs showed that the experiments can be reproduced well. The mean relative absolute deviations of the measured wall temperatures for the PDO experiments were found to be between a minimum of 0.4% and a maximum of 3.28%.

III. EXPERIMENTAL RESULTS AND DISCUSSION

III.A. Characteristics of PDO Heat Transfer

Figures 2(a) and 2(b) show characteristic steady-state temperature distributions for the PDO experiments, one for high mass flux and one for low mass flux, respectively. For both profiles, the inner wall temperature first starts around saturation temperature, and at the point where dryout occurs, the temperature starts to rise immediately with a sharp increase. For Fig. 2(a), after a maximum peak, the temperature decreases slowly, followed by a second temperature rise with a lower slope. However, for low mass flux (Fig. 2(b)), the temperature rise slows down after the sharp temperature jump, and the temperature reduction afterward is less effective. Results by Nishikawa et al. showed the same profiles for higher and lower mass velocities.[7]

In the PDO regime, the wall to vapor, wall to droplet, and vapor to droplet as well as the radiation mechanisms are responsible for the heat exchange between the wall and the two-phase fluid. First, the occurrence of the sharp temperature rise is due to the vaporization of the liquid film on the inner tube wall. Therefore, no liquid covers the wall anymore, and because of the poor heat conduction of vapor, the temperature jumps immediately. As can be seen in further experiments, the temperature still increases shortly right behind the sharp temperature rise, even for a mass flux above the transition value between 300 and 600 kg/m^2·s, e.g., Figs. 3 and 5. The reason for that is the dominant effect of the wall to vapor heat exchange due to the relatively low vapor superheat in this region. Farther downstream, the vapor still heats up, and the vapor to droplet heat exchange increases, too. That leads to droplet evaporation, which accelerates the vapor core. The result of the increased vapor velocity is an enhancement of convection, which decreases the wall temperature (Fig. 2(a)) or just slows down the rise (Fig. 2(b)).

A further explanation for the temperature reduction at high mass flux conditions is the decrease of the equilibrium vapor quality (see Sec. III.D). This on the other hand is caused by a higher turbulence of the flow. At thermal equilibrium, all liquid should be evaporated at $x_e = 1$, and the temperature should rise again. This leads to a declined cooling effect and therefore to an increase of the vapor superheat. But, because of the nonequilibrium flow, the vapor still contains entrained droplets even for equilibrium qualities above 1. Cumo et al.[8] even detected droplets in

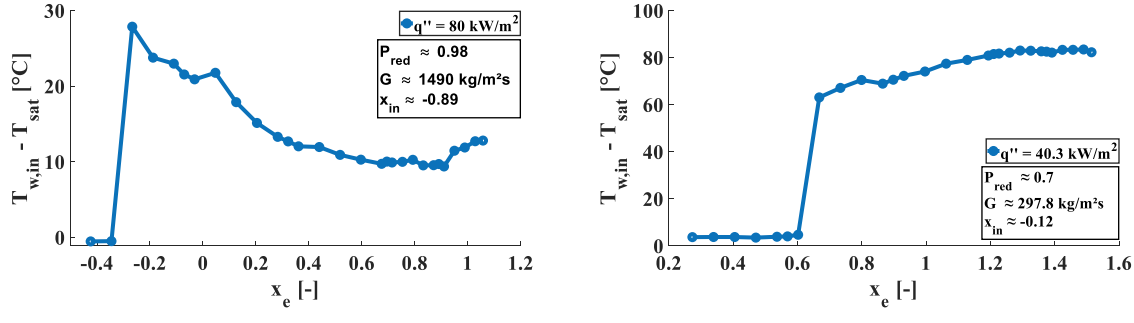

Fig. 2. Characteristic PDO temperature profile for (a) high mass flux and (b) low mass flux.

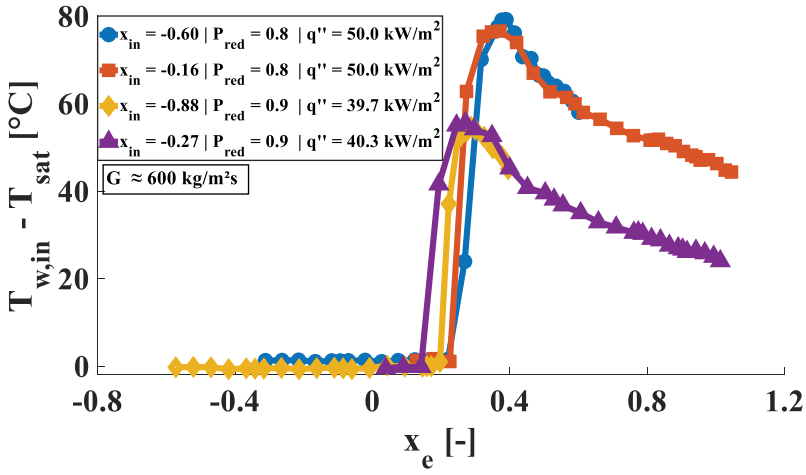

Fig. 3. Influence of the inlet quality on the PDO wall temperature distribution at two different pressures, heat fluxes, and inlet vapor qualities.

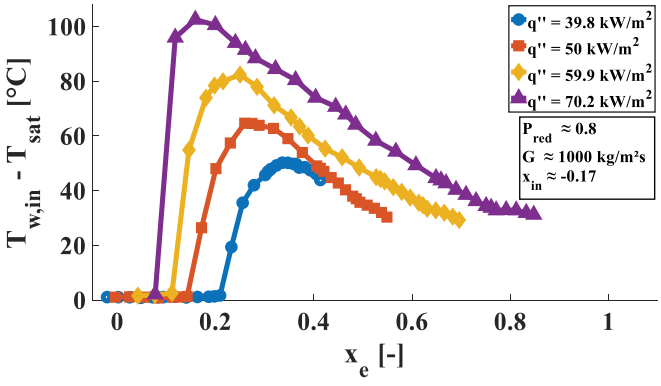

Fig. 4. Influence of heat flux on the PDO temperature distribution.

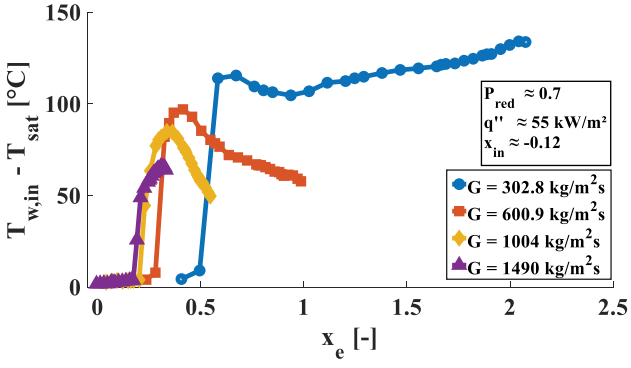

Fig. 5. Influence of mass flux on the PDO temperature distribution.

a flow with an equilibrium quality of $x_e = 2.2$. In the experiments, it could be found that the value of the equilibrium quality at which the temperature rises again depends strongly on the pressure. The higher the pressure is, the closer to unity.

III.B. Influence of Inlet Quality

This section discusses the influence of the inlet quality. Figure 3 shows two different experimental sessions, both with a mass flux of around 600 kg/m^2·s. The first session was conducted at a pressure of 3.25 MPa and a heat flux of around 50 kW/m^2, and the second session was conducted at 3.65 MPa and 40 kW/m^2. For the blue line with the round symbols and the yellow line with the diamond symbols, a subcooling temperature of 25°C was adjusted, and for the red and purple lines, a subcooling temperature of 5°C was adjusted. It may be noticed that there is no significant influence at the PDO wall temperature distribution over the vapor quality. At the pressure of 3.65 MPa, Fig. 3 shows that the critical vapor quality of the higher inlet quality is slightly shifted to a lower value. However, this can be explained by the change of the dryout occurrence inside the test tube. With higher inlet qualities, the critical point occurs closer to the entrance of the tube, and therefore, the vapor quality changes, too. With increasing vapor qualities, the profiles in the PDO region with different inlet vapor qualities will converge to one curve. Results from Nakla et al. confirm this behavior.[9]

III.C. Influence of Heat Flux

As described in Sec. II.D, after each measurement, the heat flux was increased step by step, either in steps of 2.5 kW/m^2 or in steps of 5 kW/m^2. After each step the

onset of the critical point is pulled toward the tube entrance. During this procedure the equilibrium vapor quality of the critical point is shifted toward lower values, too. This effect is shown in Fig. 4. In addition, the overall temperature profile is distributed over a wider quality range, which can be explained by Eqs. (8) and (9). Furthermore, with increasing heat flux, the overall wall temperature and the temperature peak are getting larger, without changing the slopes of the curves in the PDO region. In those experiments the heat flux was the only parameter, which was varied from around 40 to 70 kW/m^2. The other parameters, such as mass flux of 1000 kg/m^2·s, pressure of 3.25 MPa, and inlet quality of −0.07, were kept constant. Köckert et al.[6] observed the same behavior in his study.

III.D. Influence of Mass Flux

Figure 5 shows the influence of mass flux on the PDO wall temperature distribution. The heat flux, the pressure, and the inlet quality were kept constant, and only the mass flux was varied from around 300 to 1500 kg/m^2·s. Here, the heat flux is as high as possible at 55 kW/m^2 for 300 kg/m^2·s and is almost the lowest for 1500 kg/m^2·s. With increasing mass flux, the critical point is shifted upstream from the tube, and as already described in Sec. III.A, the variation of the mass flux changes the characteristic temperature distribution. The higher mass flux enhances the convection effect because of the accelerated vapor in the PDO region, as can be noticed by the temperature decrease after the temperature peak and by the value of the temperature peak itself. Therefore, higher heat flux can be adjusted to reach the wall temperature limit of 240°C, and because of that, a higher heat flux is needed to reach dryout. The transition mass flux of the characteristic profiles is between 300 and 600 kg/m^2·s.

Furthermore, Fig. 5 shows that the equilibrium quality of the critical point is lower with increasing mass flux. In addition, the entire temperature distribution shifts into lower vapor quality values. The reason for that is the higher turbulence of the flow due to the increased mass flux, which enhances the entrainment effect and thus leads to a thinner liquid film on the wall. The consequence is quicker dryout of the film and lower vapor quality, which means that more liquid will be in the vapor core and that therefore the heat transfer will be enhanced. This is the so-called inverse mass flux effect, described by Tong and Tang.[10] In the case of 300 kg/m^2·s, it can be noticed that the wall temperature slightly decreases after the temperature peak; hence, the cooling effect of the accelerated vapor can be observed as in the other three cases.

III.E. Influence of Pressure

Figures 6(a) through 6(d) show the influence of pressure on the PDO wall temperature distribution at 300, 600, 1000, and 1500 kg/m^2·s. The experiments in each figure were carried out at constant mass flux, heat flux, and subcooling temperature, and the pressure was varied. With increasing pressure, the critical vapor quality decreases to lower values, and the overall temperature profile is distributed over a wider vapor quality range. The reason for that is the change of the thermal properties of the fluid. As the pressure increases, the saturated vapor enthalpy decreases, and the enthalpy of saturated liquid increases; therefore, the heat of vaporization declines. Also noticeable is that this change is even stronger for pressures near the high subcritical pressure. The reason for that is the dramatic change of the thermal properties near the critical pressure.

Furthermore, it is observable that the whole temperature distribution as well as the temperature peak related to the dryout point decreases with an increase of pressure. That can be explained by the thermal properties as well. As mentioned before, the heat of vaporization decreases at higher pressure and is even stronger near the critical pressure, which enhances the vaporization process. Consequently, less heat is needed to reach dryout, and the temperatures in the PDO region decrease. Because of that, there is more liquid at the dryout point, and the liquid droplets evaporate more quickly because of the enhanced vaporization process.

In addition, the heat conductivity and the specific heat of the vapor phase rise sharply near the critical pressure. These affect the amount of heat that can be removed by the flow; hence, the vapor superheat decreases. Moreover, the surface tension decreases by increasing the pressure. This leads to easier droplet breakup and therefore to a smaller droplet size and a higher amount of droplets in the PDO region. According to the research of Groeneveld and Delorme[5] and Kataoka et al.,[11] it facilitates the interfacial heat transfer of the dispersed liquid droplets and the continuous vapor phase.

Cumo et al. investigations indicated that the droplet size decreases with an increase of pressure. This behavior is more pronounced in the reduced pressure range of 0.7 up to unity. For reduced pressures below 0.7, the droplet size remains almost the same.[12] Once the high pressure is combined with a mass flux above 600 to 1000 kg/m^2·s,

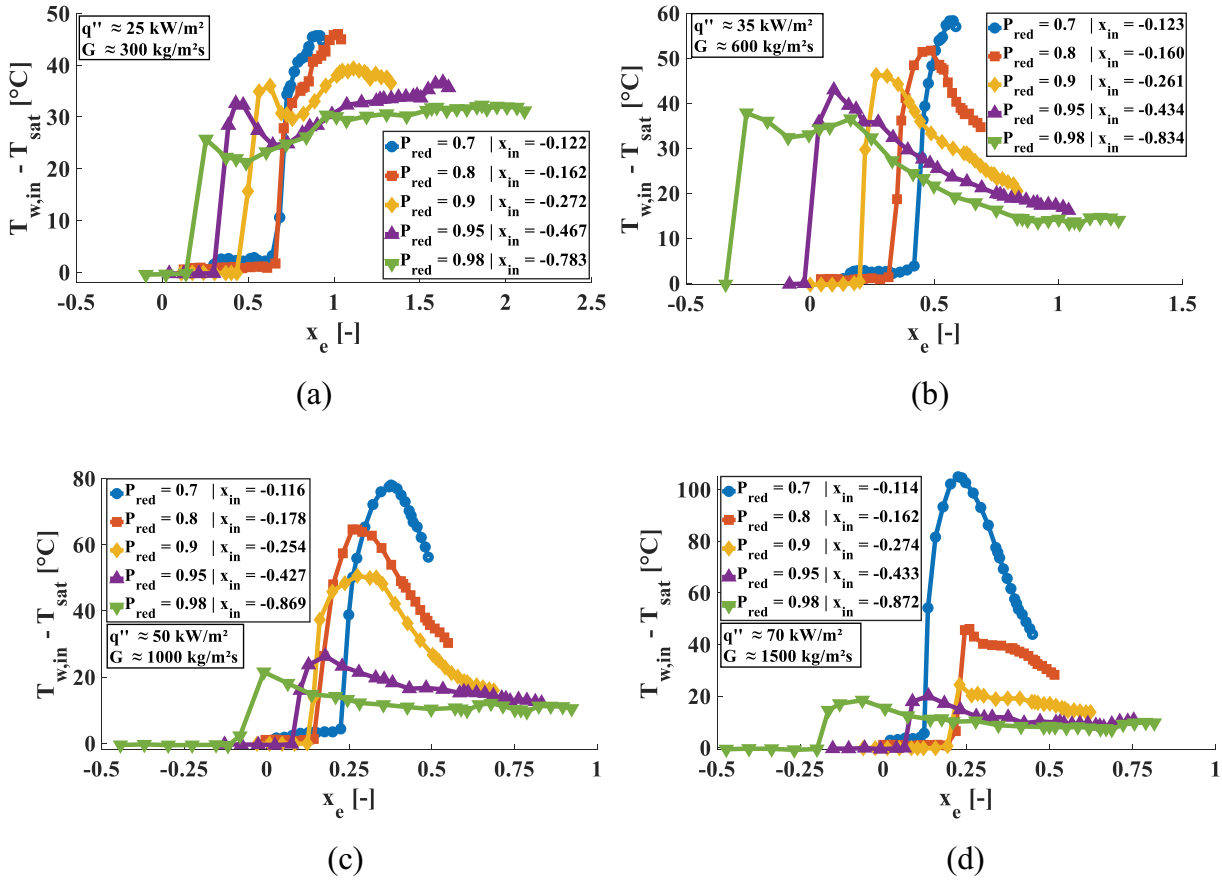

Fig. 6. Influence of pressure on the PDO temperature distribution at (a) 300 kg/m^2·s, (b) 600 kg/m^2·s, (c) 1000 kg/m^2·s, and (d) 1500 kg/m^2·s.

the influence on the temperature distribution is much stronger; this is shown in Figs. 6(c) and 6(d). Compared to the great temperature decrease associated with an increase in pressure at high mass flux conditions, the temperature decreases moderately at lower mass fluxes. Moreover, it can be observed in Fig. 6(a) that the mass flux responsible for the transition between the characteristic PDO temperature distributions shifts to lower values.

Köckert et al.[6] and Schnittger[13] got the same trend in their experiments. Mawatari and Mori[14] observed the change in the characteristic PDO profile, too. They found that the low flow rate profile changes to the high flow rate profile with increasing pressure. In addition, they observed that a small change of heat flux, mass flux, and pressure can change the PDO heat transfer characteristics strongly around the transition mass flux. Furthermore, one may notice that the higher the pressure is, the lower is the overheat of the liquid film in the annular flow before dryout occurs.

Figures 7(a) and 7(b) show again the strong influence of very high pressure. In both cases, reduced pressures of 0.7 and 0.98 were compared at three heat fluxes and a subcooling temperature of 5°C, respectively. Figure 7(a) shows the behavior at 1000 kg/m^2·s, and Fig. 7(b) shows the behavior at 1500 kg/m^2·s. Once again, one may observe that near the critical pressure, the entire wall temperature distribution strongly decreases. Another reason for that is the ratio of the saturated liquid and vapor density. Because of increasing pressure, the density ratio reduces, which decreases the void fraction, too. A minor void fraction on the other hand leads to better convective heat transfer because of lower thermal nonequilibrium and vapor superheat.[15] If the pressure is increased even closer to the critical pressure, the temperature jump related to dryout disappears. Only a slight and smooth temperature increase is then observable.[14]

IV. ASSESSMENT OF PDO HEAT TRANSFER PREDICTION METHODS

Several correlations were validated against the obtained PDO data, as discussed in this section. To ensure that only data points in the PDO region were used, the data were first filtered by a temperature and flow pattern

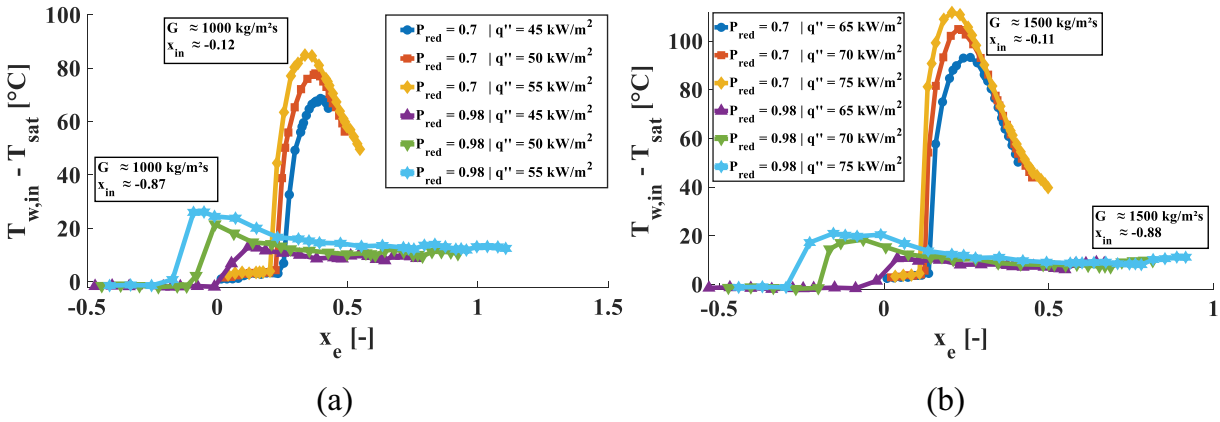

Fig. 7. Influence of pressure on the PDO temperature distribution at (a) P = 2.84 MPa and G = 1000 kg/m^2·s and (b) P = 3.98 MPa and G = 1500 kg/m^2·s.

criterion. After the filter, 10 338 PDO data points remain, which now can be used to validate the correlations. Around 20 PDO correlations were compared, and the results of four appropriate correlations were selected in this study. The results of all evaluated correlations can be found in Table A.1. In addition, a new correlation will be proposed in this section. These five correlations are suitable for very high subcritical pressure and a round tube. The correlations of Bishop et al.,[16] Miropolskiy,[17] and Groeneveld and Delorme[5] are recommended for water only, and the correlation of Song and Liu[18] and the proposed correlation are recommended for water, CO_2, and R-134a. All correlations can be used within the mass flux range investigated in this study. They all calculate the Nusselt number, which can be used to determine the HTC. The Appendix shows all tested correlations and their performance against the obtained R-134a data.

IV.A. PDO Heat Transfer Prediction Methods for High-Pressure Conditions

The first correlation of Bishop et al. is suitable for low pressure to very high pressure as well as for a wide range of different mass fluxes. The correlation uses a modified version of the Dittus-Boelter correlation with the Reynolds and Prandtl numbers at the film temperature. Additionally, the density ratio of saturated vapor and liquid as well as a quality term is taken into account. The HTC can be calculated by Eq. (12):

$$h = \frac{\lambda_f}{D_H} \cdot 0.0193 \mathrm{Re}_f^{0.8} \mathrm{Pr}_f^{1.23} \left(\frac{\rho_v}{\rho_l}\right)^{0.068} \left[x_m + \frac{\rho_v}{\rho_l}(1 - x_m)\right]^{0.68}, \quad (12)$$

where x_m = vapor mass quality, which is defined in Eq. (13),

$$x_m = \begin{cases} 0, & x_e < 0 \\ x_e, & 0 \le x_e \le 1 \\ 1, & x_e > 1 \end{cases}; \quad (13)$$

ρ_v and ρ_l = saturated densities of vapor and liquid; λ_f = heat conductivity at film temperature. The film temperature is calculated by averaging the wall and bulk temperatures. With the film temperature and the average pressure in the test section, the heat conductivity can be determined by using the National Institute of Standards and Technology reference fluid thermodynamic and transport properties database (Refprop).

The correlation of Miropolskiy, Eq. (14), can be used for low and high pressures as well as for a wide range of mass flux:

$$h = \frac{\lambda_v}{D_H} \cdot 0.023 \left[\mathrm{Re}_v \left(x_m + \frac{\rho_v}{\rho_l}(1 - x_m)\right)\right]^{0.8} \mathrm{Pr}_w^{0.8} Y \ . \quad (14)$$

It is described by the Reynolds number at a saturated vapor condition, the quality term, the Prandtl number at the wall temperature condition, and by the Miropolskiy two-phase factor Y.

The third correlation is the correlation of Song and Liu. It is suitable for water, CO_2 and R-134a and over a wide pressure range. But, for R-134a, the valid pressure range is below the range of the experiments in this study. Nevertheless, it is interesting because of its versatile parametric range. The correlation uses the Dittus-

Boelter equation with a two-phase Reynolds number, which is defined as in Eq. (15),

$$\mathrm{Re}_{TP} = \frac{G \cdot D_H}{\mu_v}\left(x_m + (1 - x_m)\frac{\mu_v}{\mu_l}\right) \quad , \tag{15}$$

and a Prandtl number at the wall temperature condition and three different correction factors. It is described by Eq. (16) with the correction factors F_1, F_2 and F_3:

$$h = \frac{\lambda_v}{D_H} \cdot F_1 \cdot F_2 \cdot F_3 \cdot \left(0.023\mathrm{Re}_{TP}^{0.8}\mathrm{Pr}_w^{0.4}\right) \quad , \tag{16}$$

where λ_v represents the heat conductivity at the vapor saturation condition.

The last correlation is from Groeneveld and Delorme. It is suitable for moderate to very high pressure and for a great mass flux range. The difference compared to the other correlations is the use of the actual vapor quality x_a instead of the equilibrium vapor quality x_e. With the help of the homogeneous void fraction α_{hom} and the nonequilibrium parameter Ψ, the actual vapor enthalpy $H_{v,a}$ and, therefore, the actual vapor quality can be calculated. With x_a and with the Reynolds and Prandtl numbers at the film temperature, the HTC can be calculated by Eq. (17):

$$h = \frac{\lambda_f}{D_H} \cdot 0.008348\left[\mathrm{Re}_f\left(x_a + \frac{\rho_v}{\rho_l}(1 - x_a)\right)\right]^{0.8774} \mathrm{Pr}_f^{0.6112} \quad . \tag{17}$$

IV.B. New PDO Heat Transfer Correlation for High-Pressure Conditions

The new proposed correlation is suitable for water, CO_2 and R-134a, but because of the dimensionless form, it can be used for all kind of fluids. Most of the PDO correlations are modified versions of the Dittus-Boelter equation, which is practical to predict the heat transfer for single-phase convective heat transfer.[19] Because of the dispersed droplet flow in the continuous vapor phase in the PDO region, the heat transfer related to droplets should also be considered, as described by Wang and Pan[20] and by Li and Anglart.[21] In the PDO region, the wall temperatures are rather low especially in the high-pressure region, and for refrigerants such as R-134a, therefore, the droplets are more likely to have a "wet contact" with the hot wall.[4] Above a minimum stable film boiling temperature, the droplets can no longer attach to the hot surface; this can also be called "dry contact."[20,22]

In addition, as pointed out in Sec. III.E, the surface tension decreases strongly by increasing the pressure, which facilitates droplet breakup. This decreases the size and increases the amount of droplets, which then leads to a larger interfacial area.[4,18] Therefore, heat transfer related to the droplets is of greater importance and will be considered here using a Weber number based on hydraulic diameter and two-phase density. The Weber number as a dimensionless number was derived by dimensionless analysis of the well-known model of Guo and Mishima.[23] The proposed correlation also consists of a modified Dittus-Boelter equation to deal with convective heat transfer.

For the development process of the new correlation, a PDO heat transfer database consisting of water, CO_2, and refrigerant was used. These experiments were also carried out in uniformly heated round tubes. The water database consists of data from Becker et al.,[24] Herkenrath et al.,[25] and Swenson et al.[26]; the refrigerant data are from Köckert et al.[27] in combination with the obtained data in this study; and the CO_2 data are from Bronik and Starflinger[28] from the University of Stuttgart. The parameter range of the data used for this new correlation can be found in Table III. During the development and the assessment, only data above a reduced pressure of 0.7 were used. Furthermore, Table IV shows the validity range of the proposed correlation and the other correlations. Equation (18) shows the proposed PDO correlation with the two-phase Reynolds number and the Prandtl number at the film temperature as well as the two-phase Weber number at saturated conditions:

$$h = \frac{\lambda_f}{D_H} \cdot 0.014\mathrm{Re}_{TP,f}^{0.7}\mathrm{Pr}_f^{1.2}\left(1 + \mathrm{We}_{TP}^{0.12}\right) \quad . \tag{18}$$

The two-phase Weber number can be calculated by Eq. (19) and is derived by the vapor Weber number in combination with the homogeneous void fraction:

$$\mathrm{We}_{TP} = \frac{G^2 D_H \rho_v}{\sigma \rho_{TP}^2} = \frac{G^2 D_H}{\sigma \rho_v}\left(x_m + (1 - x_m)\frac{\rho_v}{\rho_l}\right)^2 \quad . \tag{19}$$

IV.C. Statistical Assessment

The statistical deviation between the HTC obtained by the experiments (M) and the results of the calculation by

TABLE III

Database for the Development of the Proposed PDO Correlation

Fluid	N		P_{red}	G (kg/m^2·s)	q'' (kW/m^2)	x_e	D_H (mm)
Water	5799	Minimum	0.72	500	147	0.09	2.5
		Maximum	0.97	3500	1923	1.65	24.7
R134a	11 185	Minimum	0.7	290	11	0.001	10
		Maximum	0.98	1500	110	5.32	10
CO_2	2032	Minimum	0.7	300	15	0.07	4
		Maximum	0.99	3700	200	1.0	8

TABLE IV

Validity Range of the Introduced PDO Heat Transfer Prediction Methods

Author(s)	P_{red}	G (kg/m^2·s)	x_e	D_H (mm)
Bishop et al.	[0.185; 0.993]	[700; 3400]	[0.07; 1.0]	N/A[a]
Miropolskiy	[0.184; 1.011]	[700; 2000]	[0.06; 1.0]	[8; 24]
Groeneveld and Delorme	[0.31; 0.97]	[130; 4000]	[−0.12; 3.09]	[2.54; 20]
Song and Liu	[0.045; 0.95]	[295; 3118]	[0.001; 0.999]	[2.5; 24.7]
Proposed	[0.7; 0.99]	[290; 3700]	[0.001; 5.32]	[2.5; 24.7]

[a]N/A = Not available.

the correlations (C) were compared to each other. Table V shows the deviation in percent. Equation (A.2) calculates the error (E) of each PDO data point i. The calculated statistical parameters were then determined by Eqs. (A.3) through (A.6) in the appendix, where $\bar{\mu}_e$ = mean deviation; $\bar{\mu}_{abs}$ = mean absolute deviation; STD = standard deviation; RMS = root-mean-square value; N = number of data points.

To support Table V, the results are shown graphically in the following statistical diagrams. Because of the disagreement of the Miropolskiy correlation compared to the others, only the results of Bishop et al., Song and Liu, Groeneveld and Delorme, and the proposed prediction method are shown in Fig. 8. The mean absolute deviation and the mean deviation of Miropolskiy's results indicate that most of the HTCs are overpredicted. The standard deviation also points out that the results are widely spread.

With higher pressure, the heat transfer is significantly enhanced, and therefore, the HTC can be higher, as can be seen in Figs. 6 and 7 in Sec. III.E. This is clearly observable for reduced pressures of 0.95 and 0.98. Figure 8(a) shows the Bishop et al. correlation, which underestimates almost all HTCs at experimental values above about 2500 W/m^2·K and, therefore, mainly at high-pressure conditions, but

TABLE V

Results of the Statistical Parameters for the Introduced Correlations

Correlation	$\bar{\mu}_e$ (%)	$\bar{\mu}_{abs}$ (%)	STD (%)	*RMS* (%)	N (%)
Bishop et al.	−4.0	15.5	10.6	18.7	10 338
Miropolskiy	31.6	37.5	26.9	46.2	10 338
Groeneveld and Delorme	−0.6	19.1	13.7	23.5	10 338
Song and Liu	−44.0	44.2	13.7	46.2	10 338
Proposed	−6.2	14.0	10.2	17.3	10 338

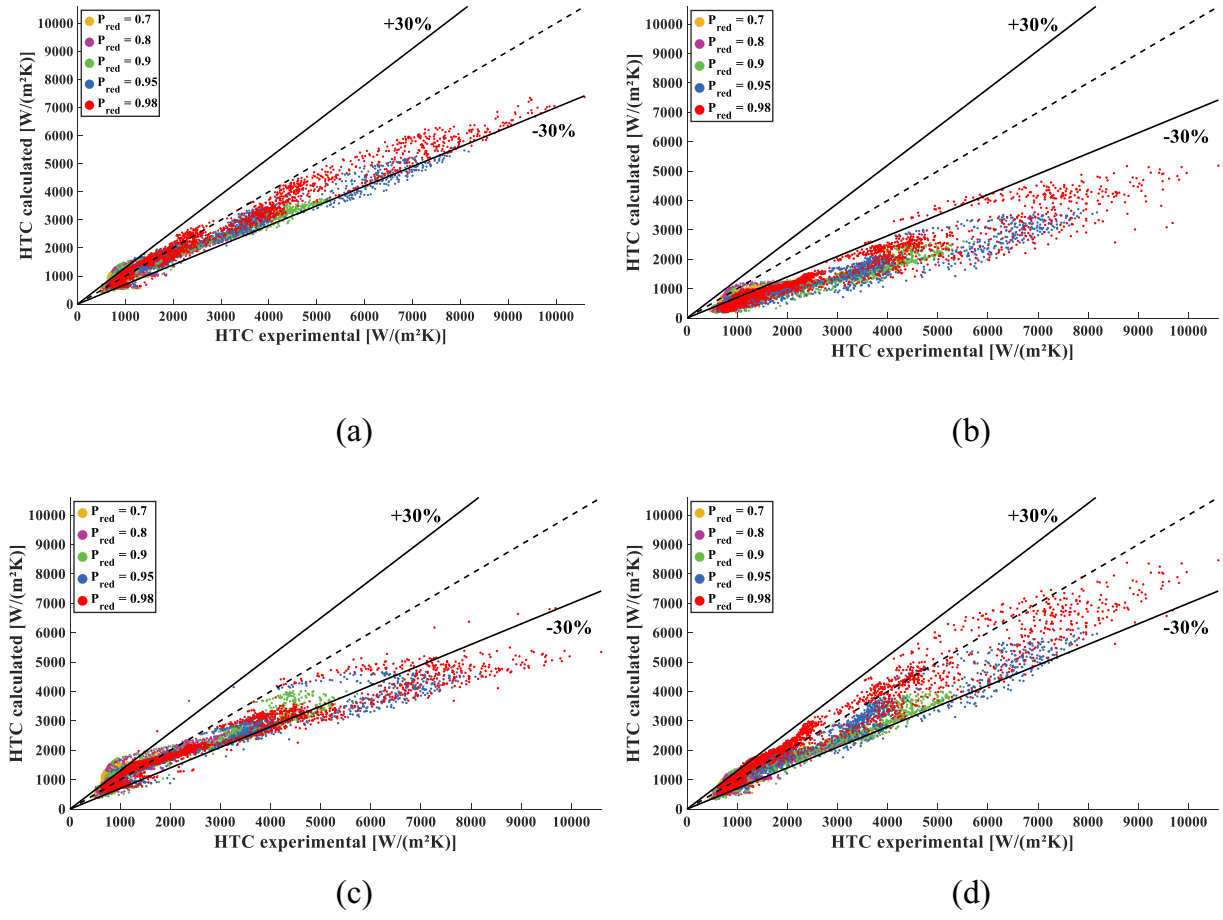

Fig. 8. Calculated HTCs with the correlation of (a) Bishop et al., (b) Song and Liu, (c) Groeneveld and Delorme, and (d) and the proposed correlation versus experimental HTCs.

shows quite good results below 2500 W/m^2·K. In general, the calculated HTC agrees well with the experimental data, and almost all calculated HTCs are within the 30% limit.

As can be seen by the results of the mean deviation and the mean absolute deviation of the Song and Liu correlation, Fig. 8(b), it can be noticed that almost all experimental HTC data points were underestimated. This correlation was developed with a wide pressure range of water, CO_2, and R-134a data, but only a few data points were in the very high-pressure region, and the maximum valid reduced pressure is 0.95. Therefore, the results of this correlation cannot be as good as the others. A detailed analysis can be seen in Sec. IV.D. However, as the standard deviation shows, the trend of the Song and Liu correlation looks good, and the calculated HTCs are not very widely spread.

Figure 8(c) shows the graphical results of the Groeneveld and Delorme model; it is noticeable that the correlation overestimates the experimental HTC below about 2000 W/m^2·K and underestimates the experimental HTCs above this value. That is supported by comparing the mean relative deviation and the mean relative absolute deviation. The $\bar{\mu}_e$ value would rate the correlation as pretty good, but the $\bar{\mu}_{abs}$ value shows that the predicted HTC partially deviates more from the real value. In general, all three prediction methods have some problems, especially in predicting high HTC in the high-pressure region; see also Sec. IV.D.

Figure 8(d) shows the results of the proposed prediction method. The mean deviation and Fig. 8(d) indicate that this correlation underpredicts the HTC slightly, but in general, the calculated HTC has the best agreement regarding the calculated HTC. This can be confirmed by the standard deviation of 10.2% and an overall well mean absolute deviation of 14%. Furthermore, the correlation shows better agreement in the high-pressure region in combination with high HTC values compared with the other correlations. Figures 9(a) and 9(b) show the PDO wall temperature distribution for a few selected experimental cases with R-134a. In addition, the wall temperatures calculated by the proposed correlation are also included, and the results again indicate good agreement.

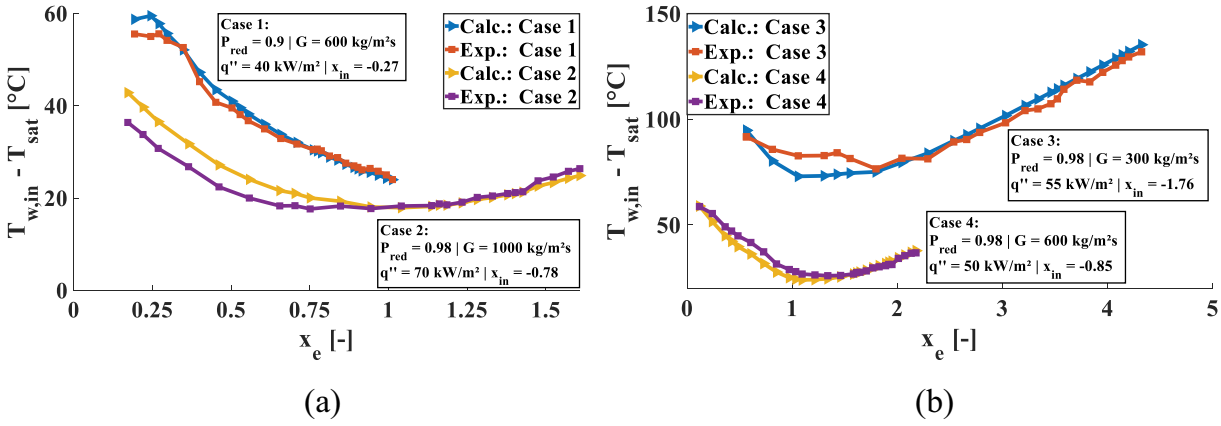

Fig. 9. Post-dryout wall temperature distributions of the experimental measurement compared to the distribution calculated by the proposed correlation.

IV.D. More Detailed Statistical Assessment

To have a more detailed assessment of the PDO prediction methods, the deviations depending on pressure and mass flux were determined and are shown in Figs. 10 and 11. The correlations of Song and Liu and of Miropolskiy are not mentioned here because of the outperformance of the other correlations. But, for the sake of completeness, the results are also displayed in Fig. 12. As shown in Table V, the mean deviations of the proposed correlation and the Bishop et al. correlation are very similar and have the best mean absolute deviation. But, a more detailed analysis shows that both differ depending on the pressure, as can be seen in Fig. 10(a). The Bishop et al. correlation overpredicts the HTC first, and with increasing pressure, it underpredicts the experimental results.

In comparison, the proposed correlation always underpredicts the experimental HTC slightly, except for a reduced pressure of 0.98. In this case, it overpredicts the result with a deviation of 1.8%. In addition, the Groeneveld and Delorme prediction method shows a very good mean deviation, but Fig. 10(a) reveals that the method first overpredicts the HTC for lower reduced pressures of 0.7 and 0.8 and that with increasing pressure, the results were underpredicted, similar to the results of the Bishop et al. correlation. Figure 10(b) presents the RMS results of the different correlations for different reduced pressures. The results show that the proposed correlations not only are generally closer to the real experimental results compared to the other correlations but also are closer for each of the reduced pressures that were investigated in this study.

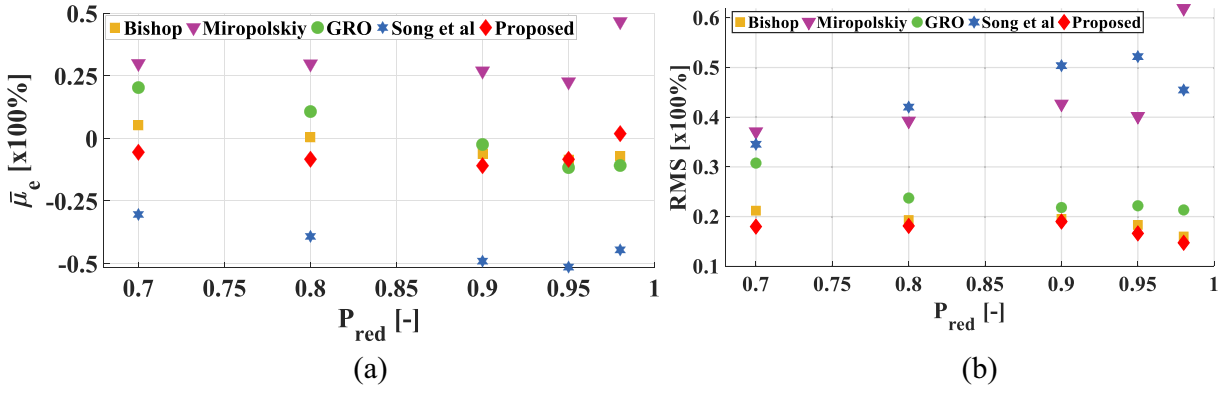

Fig. 10. Distribution of (a) mean deviation and (b) RMS versus reduced pressure for the different PDO correlations. GRO = Groeneveld and Delorme.

In addition, to support the results of the proposed correlation, Fig. 11 shows the error distributions of the HTC prediction methods for the different reduced pressures and mass fluxes. The error bars of the proposed correlation show predominantly smaller error distributions compared to the others, which is supported by the values of the standard deviation. Furthermore, Fig. 11(b) also shows good agreement of the proposed correlation depending on the mass fluxes. For mass fluxes up to 1000 kg/m^2·s, the HTCs were somewhat underpredicted and for 1500 kg/m^2·s were slightly overpredicted with 4.6%. A comparison of the error bars indicates again that the HTC predictions of the proposed correlation show in general the best agreement.

Figure 12 shows the mean deviations of the five correlations versus a range of HTC values. The HTC ranges were determined by a rounded maximum HTC value for each of the pressures presented in this study. To support Fig. 12, Table VI also presents the results. As can be seen, the number of data points N decreases with an increase of HTC range. In general, the mean absolute deviations of the prediction methods start to get worse with increasing HTC values. This assessment shows again the problem of predicting high HTCs, which are mostly related to high pressure. The Song and Liu correlation are again not satisfactory, and the Miropolskiy correlation shows somewhat good results (HTC = 3800 to 5700), however very inconsistent. The Groeneveld and Delorme model also shows worse results at higher HTC. The proposed correlation and the Bishop et al. correlation can predict the high experimental HTC the best, but the proposed correlation provides much better results, especially for high HTC. Therefore, the new proposed

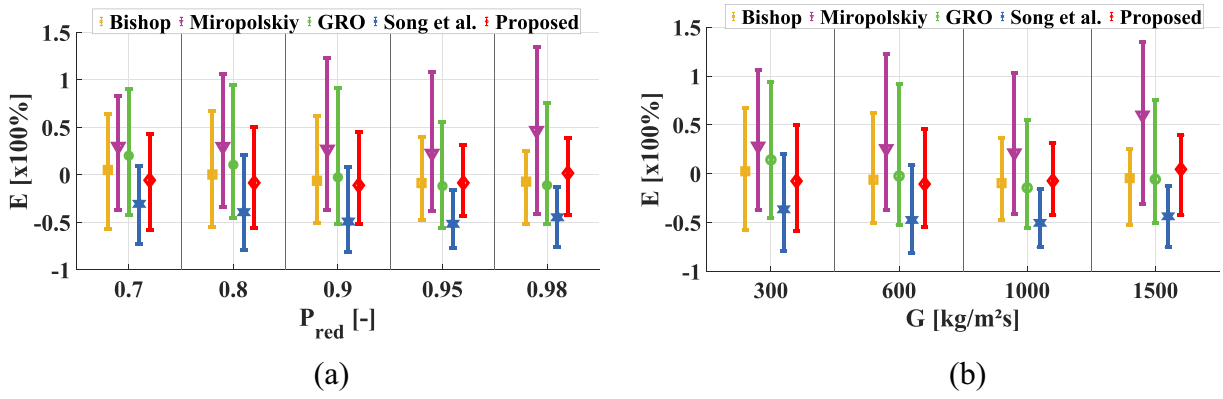

Fig. 11. Error distribution of the different PDO correlations versus (a) the reduced pressure and (b) the mass flux. GRO = Groeneveld and Delorme.

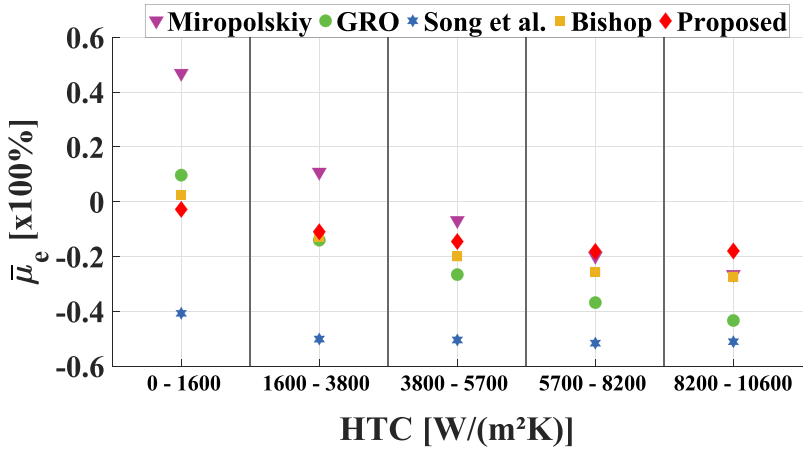

Fig. 12. Distribution of the mean deviation versus HTC ranges for the different PDO correlations. GRO = Groeneveld and Delorme.

TABLE VI

Mean Deviations Versus HTC Ranges Related to Fig. 12

	HTC Range [W/(m^2·K)]				
	0 to 1600	1600 to 3800	3800 to 5700	5700 to 8200	8200 to 10 600
	N = 6803	N = 2222	N = 814	N = 437	N = 62
Correlation	$\bar{\mu}_e$ (%)				
Bishop et al.	2.4	−12.7	−20.0	−25.6	−27.3
Miropolskiy	46.9	10.8	−6.8	−19.9	−26.5
Groeneveld and Delorme	9.7	−14.1	−26.6	−36.8	−43.4
Song and Liu	−40.7	−50.1	−50.5	−51.6	−51.1
Proposed	−2.8	−10.9	−14.6	−18.2	−18.0

prediction method can be recommended to predict heat transfer in the PDO region for high to very high subcritical pressure conditions.

V. CONCLUSION

Steady-state PDO experiments were conducted at the KIMOF, using the refrigerant R-134a in a vertical uniformly heated round tube. The experiments were done at high subcritical pressure, and the results were used to assess four suitable PDO correlations as well as a new developed correlation. The results can be summarized as follows:

1. The experimental PDO temperature distributions showed good agreement with the profiles found in the literature. There are two characteristic PDO temperature distributions, one for mass flux conditions above a transition range of 300 to 600 kg/m^2·s and one below. This transition range changes to lower values with increasing pressure.

2. It was confirmed that the inlet vapor quality has no significant influence on the PDO temperature distribution. The PDO temperature curves with different inlet vapor qualities (other flow conditions remain the same) converge at vapor qualities greater than the critical vapor quality.

3. The increasing heat flux leads to higher temperature peaks as well as an overall higher temperature distribution. In addition, the entire temperature profile is distributed over a wider equilibrium vapor quality range.

4. Increasing the mass flux reduces the temperature distribution, and the onset of the dryout point is shifted to lower qualities. The inverse mass flux effect, described by Tong and Tang, was also confirmed.

5. As the pressure increases, the entire temperature distribution and the temperature peak after the dryout point decrease strongly. This effect is even stronger near the critical pressure. Because of the drastic change of the thermal fluid properties at high subcritical pressure, the heat flux to reach the dryout point decreases. In addition, the critical vapor quality decreases, too. Moreover, it was found that the effect of increasing pressure is even stronger in combination with a mass flux above 1000 kg/m^2·s.

6. A new PDO correlation suitable for high pressures and a great mass flux range was developed that considers the heat transfer related to droplets. To do that, a two-phase Weber number was derived and combined with a modified Dittus-Boelter correlation.

7. The literature review and the data analysis show that droplet behavior, especially in the high-pressure region, has to be considered because it plays a relevant role in the overall heat transfer in the PDO region.

8. In R-134a, 10 338 PDO data points were used to validate the four suitable correlations and the new proposed correlation. In general, the Groeneveld and Delorme model and the Bishop et al. correlation showed good results but had some problems in predicting the high HTC for high-pressure conditions. However, the proposed correlation can predict the HTC well, regardless of the pressure condition.

9. More experiments are planned in the future, and with additional data from the literature, the new proposed PDO correlation will be further improved and extended.

APPENDIX

STATISTICAL ASSESSMENT

Table A.1 contains the PDO heat transfer prediction methods and the calculated statistical deviations against the obtained data in this study.

TABLE A.1.

Results of all Evaluated PDO Heat Transfer Prediction Methods and their Statistical Errors

Author(s)	Correlation	$\bar{\mu}_e$ (%)	STD (%)	RMS (%)
Polomik[29]	$h = \frac{\lambda_v}{D_H} 0.00115 (\mathrm{Re}_v)^{0.9} \mathrm{Pr}_v^{0.3} \left(\frac{T_w}{T_{sat}} - 1\right)$	−46.4	17.9	50.5
Polomik[29]	$h = \frac{\lambda_v}{D_H} 0.0039 \left[\mathrm{Re}_v \left(x_e + \frac{\rho_v}{\rho_l}(1 - x_e)\right)\right]^{0.9}$	−17.7	18.0	30.2
Bishop et al.[16]	$h = \frac{\lambda_f}{D_H} 0.0193 \mathrm{Re}_f^{0.8} \mathrm{Pr}_f^{1.23} \left(\frac{\rho_v}{\rho_l}\right)^{0.088} \left[x_e + \frac{\rho_v}{\rho_l}(1 - x_e)\right]^{0.68}$	−4.0	10.6	18.7
Bishop et al.[16]	$h = \frac{\lambda_w}{D_H} 0.033 \mathrm{Re}_w^{0.8} \mathrm{Pr}_w^{1.25} \left(\frac{\rho_v}{\rho_l}\right)^{0.197} \left[x_e + \frac{\rho_v}{\rho_l}(1 - x_e)\right]^{0.738}$	19.6	16.9	28.9
Bishop et al.[30]	$h = \frac{\lambda_w}{D_H} 0.098 \left[\mathrm{Re}_w \frac{\rho_{v,w}}{\rho_v} \left(x_e + \frac{\rho_v}{\rho_l}(1 - x_e)\right)\right]^{0.8} \mathrm{Pr}_w^{0.83} \left(\frac{\rho_v}{\rho_l}\right)^{0.5}$	52.8	25.6	58.9
Miropolskiy[17]	$h = \frac{\lambda_v}{D_H} 0.023 \left[\mathrm{Re}_v \left(x_e + \frac{\rho_v}{\rho_l}(1 - x_e)\right)\right]^{0.8} \mathrm{Pr}_w^{0.8} Y$ $Y = 1 - 0.1 \left(\frac{\rho_v}{\rho_l} - 1\right)^{0.4} (1 - x_e)^{0.4}$	31.6	26.9	46.2
Herkenrath et al.[25]	$h = \frac{\lambda_w}{D_H} 0.06 \left[\mathrm{Re}_w \left(x_e + \frac{\rho_v}{\rho_l}(1 - x_e)\right) \left(\frac{\rho_{v,w}}{\rho_v}\right) \mathrm{Pr}_w\right]^{0.8} \left(\frac{G}{1000 \frac{\mathrm{kg}}{\mathrm{m}^2 \cdot \mathrm{s}}}\right)^{0.4} \left(\frac{P}{P_c}\right)^{2.7}$	−7.3	16.1	24.8
Slaughterbeck et al.[31]	$h = \frac{\lambda_v}{D_H} 0.0001604 \left[\mathrm{Re}_v \left(x_e + \frac{\rho_v}{\rho_l}(1 - x_e)\right)\right]^{0.838}$ $\mathrm{Pr}_w^{1.81} \varsigma^{0.278} \left(\frac{P}{P_c}\right)^{-0.508}, \varsigma \text{ in } \frac{\mathrm{Btu}}{\mathrm{h \cdot ft}^2}$	−75.2	4.8	75.3
Groeneveld and Moeck[32]	$h = \frac{\lambda_v}{D_H} a \left[\mathrm{Re}_v \left(x_e + \frac{\rho_v}{\rho_l}(1 - x_e)\right)\right]^b \mathrm{Pr}_w^c Y^d \phi^e$ $Y = 1 - 0.1 \left(\frac{\rho_v}{\rho_l} - 1\right)^{0.4} (1 - x_e)^{0.4}$			
1[32]	$a = 0.000185, b = 1.0, c = 1.57, d = -1.12, e = 0$	−90.1	3.5	90.1
2[32]	$a = 0.00109, b = 0.989, c = 1.41, d = -1.15, e = 0$	−25.8	13.0	29.9
3[32]	$a = 0.00327, b = 0.901, c = 1.32, d = -1.5, e = 0$	31.6	26.9	46.2
Swenson et al.[26]	$h = \frac{\lambda_w}{D_H} 0.076 \left[\mathrm{Re}_v \left(x_e + \frac{\rho_v}{\rho_l}(1 - x_e)\right) \left(\frac{\rho_{v,w}}{\rho_v}\right)\right]^{0.8} \mathrm{Pr}_w^{0.8}$	100.7	61.8	118.3

(Continued)

TABLE A.1. (Continued)

Author(s)	Correlation	$\bar{\mu}_e$ (%)	STD (%)	RMS (%)
Groeneveld and Delorme[5]	$h = \frac{\lambda_f}{D_H} 0.008348 \left[\mathrm{Re}_f \left(x_a + \frac{\rho_v}{\rho_l}(1-x_a) \right) \right]^{0.8774} \mathrm{Pr}_f^{0.6112}$ $x_a = \frac{\Delta H_{v,l}}{H_{v,a} - H_l} x_e, h_{v,a} = \exp\left(-tan(\psi) - (3\alpha_{hom})^{-4} \right) \Delta H_{v,l} +$ $H_l, \mathrm{Re}_{hom} = \frac{G D_H x_m}{\mu_v \alpha_{hom}}$ $\psi = 0.13864 \mathrm{Pr}_v^{0.2031} \mathrm{Re}_{hom}^{0.20006} \left(\frac{q'' D_H C_{p,v}}{\lambda \Delta H_{v,l}} \right)^{-0.9232}$ $\left(1.3072 - 1.0833 x_e + 0.8455 x_e^2 \right)$	−0.6	13.7	23.5
Nishikawa et al.[33]	$h = \frac{\lambda_v}{D_H} 0.0048 \left[\frac{G D_H}{\mu_v} \left(x_a + \frac{\rho_v}{\rho_l}(1-x_a) \right) \right]^{0.92} \mathrm{Pr}_v^{0.4} \left(1 + \frac{2.0}{\left(\frac{L}{D_H} \right)^{1.1}} \right)$ $T_{v,a} - T_{sat} = \frac{H_{v,a} - H_v}{C_{p,v}} = \frac{\Delta H_{v,l}}{C_{p,v}} \left(\frac{x_e}{x_a} - 1 \right), \frac{dx_a}{dx_e} = \frac{1}{\mathrm{Bo} \cdot \mathrm{Kn}} \left(\frac{x_e}{x_a} - 1 \right)$ $\mathrm{Bo} = \frac{q''}{G \Delta H_{v,l}}, \mathrm{Kn} = 4260 \left(\frac{G D_H}{\mu_v} \right)^{0.52} \left(\frac{G^2 D_H}{\alpha \rho_v} \right)^{-0.73} \left(\mathrm{Pr}_v \frac{\rho_v}{\rho_l} \right)^{0.3}$ $x_a^n (1-x_a)^{-0.2} \left(\frac{x_e}{x_a} - 1 \right)^{0.83}$ $n = 2.0 \exp\left[-1.3 \left(\frac{G \mu_v}{\sigma \rho_v} \right) \left(\frac{\rho_l}{\rho_v} - 1 \right)^{1.7} \right] - 1$	47.4	25.4	51.2
Plummer et al.[34]	$h = \frac{\lambda_v}{D_H} 0.033 \left(\frac{G x_a D_H}{\mu_a} \right)^{0.8} \mathrm{Pr}_v^{\frac{1}{3}} \left(\frac{\mu_v}{\mu_{v,w}} \right)^{0.14} \left[1 + 0.3 \left(\frac{D_H}{0.01 D_H + L_{FB}} \right)^{0.7} \right]$	−10.4	44.3	68.3
Chen et al.[3]	$h = \frac{\lambda_f}{D_H} \frac{F}{2} G x_a C_{p,v} \mathrm{Pr}_f^{-\frac{2}{3}}, \frac{x_a}{x_e} = 1 - B(P) T_d, T_d = \frac{T_{v,a} - T_{sat}}{T_w - T_{v,a}}$ $F = 0.037 \left[\frac{D_H G}{\mu_v} \left(x_a - \frac{\rho_v}{\rho_l}(1-x_a) \right) \right]^{-0.17}, B(P) = \frac{0.26}{1.15 - \left(\frac{P}{P_c} \right)^{0.65}}$	−4.4	20.8	36.8
Ünal and Van Gasselt[35]	$h = \frac{\lambda_f}{D_H} 0.0091 a_1 a_2 a_3 a_4 a_5 a_6 a_7 a_8$ $a_1 = \left[\frac{G D_H}{\mu_f} \left(x_e + \frac{\rho_v}{\rho_l}(1-x_e) \right) \right]^{1.154},$ $a_2 = \mathrm{Pr}_\mathrm{f}^{0.577}, \mathrm{a}_3 = \left(\frac{\lambda_\mathrm{f}}{\lambda_\mathrm{c}} \right)^{0.595}, \mathrm{a}_4 = \left(\frac{\mathrm{T_f}}{\mathrm{T_c}} \right)^{-2.17}$ $a_5 = \left(\frac{P}{P_c} \right)^{0.212} \left(1 - \frac{P}{P_c} \right)^{-0.27}, a_6 = \left[\frac{G^2}{\rho_l^2 D_H g} \right]^{0.0396},$ $a_7 = \left[\frac{q''}{G H_l} \right]^{0.44}, a_8 = 1$	−22.7	14.9	28.9
Koizumi et al.[36]	$\frac{h}{h_{GRO}} = (-35 x_e + 42) \exp\left(-\frac{T_w - T_{sat}}{-35K \cdot x_e + 66K} \right) + 1.5$	85.2	57.9	103.0
Rohsenow[37]	$h = \frac{\lambda_f}{D_H} 0.00835 \left(\frac{G x_a D_H}{\mu_f \alpha_s} \right)^{0.8774} \mathrm{Pr}_f^{0.6112} R_{\mathrm{Nu}}$ α_s : *Void fraction calculated with slip according to the model* R_{Nu} : *Nusselt − Number Ratio versus actual quality curve*	−23.5	13.5	28.6
Song and Liu[18]	$h = \frac{\lambda_v}{D_H} F_1 F_2 F_3 \left(0.023 \mathrm{Re}_{TP}^{0.8} \mathrm{Pr}_w^{0.4} \right)$ $F_1 = 0.008346 \mathrm{Re}_{TP}^{0.319}, F_2 = \max\left(0.795 \mathrm{Pr}_w^{-1.752}, 0.809 \mathrm{Pr}_w^{1.287} \right)$ $F_3 = \begin{cases} 0.715(1-x_e)^{0.678}, & x_e < 0.4 \\ 1.0 & , x_e \geq 0.4 \end{cases}, \mathrm{Re}_{TP} = \frac{G D_H}{\mu_v} \left[x_m + \frac{\mu_v}{\mu_l}(1-x_m) \right]$	−44.0	13.7	46.2

The following equations calculate the statistical deviation between the HTC obtained by the experiments and the results of the calculation by the PDO heat transfer prediction methods.

$$E_i = \frac{C_i - M_i}{M_i} \tag{A.2}$$

$$\bar{\mu}_e = \frac{1}{N}\sum_{i=1}^{N} E_i \tag{A.3}$$

$$\bar{\mu}_{abs} = \frac{1}{N}\sum_{i=1}^{N} |E_i| \tag{A.4}$$

$$\mathrm{STD} = \sqrt{\frac{1}{N}\sum_{i=1}^{N} (E_i - \bar{\mu}_e)^2} \tag{A.5}$$

$$\mathrm{RMS} = \sqrt{\frac{1}{N}\sum_{i=1}^{N} E_i^2}. \tag{A.6}$$

Nomenclature

Bo = boiling number
C = correlated data point
C_p = specific heat (J/kg·K)
D = diameter (m)
E = error (%)
F = correction factor
G = mass flux (kg/m^2·s)
H = enthalpy (kJ/kg)
h = heat transfer coefficient (W/m^2·K)
I = current (A)
L = length (m)
M = measured data point
m = mass flow rate (kg/s)
N = number of data points
P = pressure (bar)
Pr = Prandtl number
P_{red} = reduced pressure
Q = heat (W)
Q_{loss} = heat loss (W)
q'' = heat flux (kW/m^2)
q''' = volumetric heat flux (kW/m^3)
Re = Reynolds number
RMS = root-mean-square value (%)
r = radius (m)
s = wall thickness (m)
STD = standard deviation (%)
T = temperature (°C)
U = voltage (V)
We = Weber number
x = quality
x_m = mass quality
Y = Miropolskiy factor
z = relative length

Greek

α = void fraction
λ = thermal conductivity (W/m·K)
μ = dynamic viscosity (N·s/m^2)
$\bar{\mu}_e$ = mean deviation (%)
ρ = density (kg/m^3)
σ = surface tension (N/m)
Ψ = nonequilibrium parameter

Subscript

a = actual
c = critical
e = equilibrium
f = film region
H = heated
hom = homogeneous
I = point of interest
i = data point
in = inner
l = liquid phase
out = outer
sat = saturation
TP = two phase

u = environment

v = vapor phase

w = wall

Acknowledgments

The authors would like to thank the German Federal Ministry of Education and Research (BMBF, CPC-HD Project, grant number 02NUK062A) for providing the financial support for this study.

Funding

This work was supported by the Bundesministerium für Bildung und Forschung [02NUK062A].

Disclosure Statement

No potential conflict of interest was reported by the author(s).

ORCID

Nikolai Rensch http://orcid.org/0009-0003-3037-0037

References

1. B. R. VIJAYARANGAN, S. JAYANTI, and A. R. BALAKRISHNAN, "Studies on Critical Heat Flux in Flow Boiling at Near Critical Pressures," *Int. J. Heat Mass Transfer*, **49**, *1–2*, 259 (2006); https://doi.org/10.1016/j.ijheatmasstransfer.2005.06.029.
2. A. F. VARONE Jr. and W. M. ROHSENOW, "Post Dryout Heat Transfer Prediction," *Nucl. Eng. Des.*, **95**, 315 (1986); https://doi.org/10.1016/0029-5493(86)90057-9.
3. J. C. CHEN, F. T. OZKAYNAK, and R. K. SUNDARAM, "Vapor Heat Transfer in Post-CHF Region Including the Effect of Thermodynamic Non-Equilibrium," *Nucl. Eng. Des.*, **51**, *2*, 143 (1979); https://doi.org/10.1016/0029-5493(79)90086-4.
4. D. C. GROENEVELD, "Post-Dryout Heat Transfer: Physical Mechanisms and a Survey of Prediction Methods," *Nucl. Eng. Des.*, **32**, *3*, 283 (1975); https://doi.org/10.1016/0029-5493(75)90099-0.
5. D. C. GROENEVELD and G. G. J. DELORME, "Prediction of Thermal Non-Equilibrium in the Post-Dryout Regime," *Nucl. Eng. Des.*, **36**, *1*, 17 (1976); https://doi.org/10.1016/0029-5493(76)90138-2.
6. L. KÖCKERT et al., "Studies on Post-Dryout Heat Transfer in R-134a Vertical Flow," *Int. J. Adv. Nucl. Reactor Des. Technol.*, **3**, 44 (2021); https://doi.org/10.1016/j.jandt.2021.05.001.
7. K. NISHIKAWA et al., "An Experiment on the Heat Transfer Characteristics in the Post-Burnout Region at High Subcritical Pressures," *Nucl. Eng. Des.*, **74**, *2*, 233 (1982); https://doi.org/10.1016/0029-5493(83)90060-2.
8. M. CUMO, G. FERRARI, and G. E. FARELLO, "A Photographic Study of Two-Phase Highly Dispersed Flows," Comitato Nazionale l'Energia Nucleare (1971).
9. M. E. NAKLA, D. C. GROENEVELD, and S. C. CHENG, "Experimental Study of Inverted Annular Film Boiling in a Vertical Tube Cooled by R-134a," *Int. J. Multiphase Flow*, **37**, *1*, 67 (2011); https://doi.org/10.1016/j.ijmultiphaseflow.2010.08.006.
10. L. S. TONG and Y. S. TANG, *Boiling Heat Transfer and Two-Phase Flow*, p. 369, CRC Press, Boca Raton, Florida (1997).
11. I. KATAOKA, M. ISHII, and K. MISHIMA, "Generation and Size Distribution of Droplet in Annular Two-Phase Flow," *J. Fluids Eng.*, **105**, *2*, 230 (1983); https://doi.org/10.1115/1.3240969.
12. M. CUMO et al., "On Two-Phase Highly Dispersed Flows," Comitato Nazionale l'Energia Nucleare (1974).
13. R. B. SCHNITTGER, "Untersuchungen zum Wärmeübergang bei vertikalen und horizontalen Rohrströmungen im post-dryout Bereich," Dissertation, University Hannover (Jan. 1982).
14. T. MAWATARI and H. MORI, "An Experimental Study on Characteristics of Post-CHF Heat Transfer in the High Subcritical Pressure Region Near to the Critical Pressure," *J. Therm. Sci. Technol.*, **11**, *1*, 1 (2016); https://doi.org/10.1299/jtst.2016jtst0006.
15. S. K. LEE and S. H. CHANG, "Experimental Study of Post-Dryout with R-134a Upward Flow in Smooth Tube and Rifled Tubes," *Int. J. Heat Mass Transfer*, **51**, *11–12*, 3153 (2008); https://doi.org/10.1016/j.ijheatmasstransfer.2007.08.026.
16. A. A. BISHOP, R. O. SANDBERG, and L. S. TONG, "Forced Convection Heat Transfer at High Pressures After the Critical Heat Flux," *Proc. ASME-AIChE Heat Transfer Conf.* Los Angeles, California, August 8–11, 1965, ASME Paper 65-HT-31, American Society of Mechanical Engineers (1965).
17. Z. L. MIROPOLSKIY, "Heat Transfer in Film Boiling of Steam Water Mixture in Steam Generation Tubes," *Teploenergetika*, **10**, *5*, 49 (1963).
18. M. SONG and X. LIU, "Assessment of CHF and Post-CHF Heat Transfer Models for High-Pressure Condition," *Front.*

Energy Res., **9** (2021); https://doi.org/10.3389/fenrg.2021.782086.

19. W. H. MCADAMS et al., "Heat Transfer at High Rates to Water with Surface Boiling," *Ind. Eng. Chem.*, **41**, *9*, 1945 (1949); https://doi.org/10.1021/ie50477a027.
20. Y. J. WANG and C. PAN, "A One-Dimensional Semi-Empirical Model Considering Transition Boiling Effect for Dispersed Flow Film Boiling," *Nucl. Eng. Des.*, **316**, 99 (2017); https://doi.org/10.1016/j.nucengdes.2017.03.004.
21. H. LI and H. ANGLART, "Prediction of Dryout and Post-Dryout Heat Transfer Using a Two-Phase CFD Model," *Int. J. Heat Mass Transfer*, **99**, 839 (2016); https://doi.org/10.1016/j.ijheatmasstransfer.2016.04.021.
22. J. BREITENBACH, I. V. ROISMAN, and C. TROPEA, "Heat Transfer in the Film Boiling Regime: Single Drop Impact and Spray Cooling," *Int. J. Heat Mass Transfer*, **110**, 34 (2017); https://doi.org/10.1016/j.ijheatmasstransfer.2017.03.004.
23. Y. GUO and K. MISHIMA, "A Non-Equilibrium Mechanistic Heat Transfer Model for Post-Dryout Dispersed Flow Regime," *Exp. Therm. Fluid Sci.*, **26**, *6–7*, 861 (2002); https://doi.org/10.1016/S0894-1777(02)00195-4.
24. K. M. BECKER et al., "An Experimental Investigation of Post Dryout Heat Transfer," Royal Institute of Technology Stockholm (May 1983).
25. H. HERKENRATH et al., "Wärmeübergnag an Wasser bei Erzwungener Strömung im Druckbereich von 140 bis 250 bar," EUR-3658, European Atomic Energy Community (1967).
26. H. S. SWENSON, J. R. CARVER, and G. SZOEKE, "The Effect of Nucleate Boiling Versus Film Boiling on Heat Transfer in Power Boiler Tubes," *J. Eng. Gas Turbines Power*, **84**, *4*, 365 (1962); https://doi.org/10.1115/1.3675052.
27. L. KÖCKERT et al., "Experimental Study of Post-Dryout Heat Transfer and Rewetting in an R-134a Cooled Vertical Tube at Comparable Water-Cooled Reactor Pressure Conditions," Presented at 12th International Topical Meeting on Nuclear Reactor Thermal-Hydraulics, Operation and Safety, Qingdao, China, October 14–18, 2018.
28. J. BRONIK and J. STARFLINGER, Institute of Nuclear Technology and Energy Systems (IKE), University of Stuttgart, Convective Heat Transfer and Critical Heat Flux in CO_2 at High Subcritical Pressures, Personal Communication (2023).
29. E. E. POLOMIK, "Transition Boiling Heat Transfer Program. Final Summary Report on Program for February 1963–October 1967," GEAP-5563, General Electric Company (Jan. 1967).
30. A. A. BISHOP, R. O. SANDBERG, and L. S. TONG, "High-Temperature Supercritical Pressure Water Loop. Part V. Forced Convection Heat Transfer to Water After the Critical Heat Flux at High Supercritical Pressures," WCAP-2056, Westinghouse Electric Corporation (1964).
31. D. C. SLAUGHTERBECK, L. J. YBARRONDO, and C. F. OBENCHAIN, "Flow Film Boiling Heat Transfer Correlations: A Parametric Study with Data Comparisons," CONF-730803-5, Aerojet Nuclear Company (Aug. 1973).
32. D. C. GROENEVELD and E. O. MOECK, "An Investigation of Heat Transfer in the Liquid Deficient Regime," AECL-3281, Atomic Energy of Canada Limited, Chalk River Nuclear Laboratories (Dec. 1969).
33. K. NISHIKAWA et al., "Post-Dryout Heat Transfer to Freon in a Vertical Tube at High Subcritical Pressures," *Int. J. Heat Mass Transfer*, **29**, *8*, 1245 (1986); https://doi.org/10.1016/0017-9310(86)90157-2.
34. D. N. PLUMMER, P. GRIFFITH, and W. M. ROHSENOW, "Post-Critical Heat Transfer to Flowing Liquid in a Vertical Tube," *Trans. Canadian Soc. Mech. Eng.*, **4**, 3 (1976); https://doi.org/10.1139/tcsme-1976-0022.
35. H. C. ÜNAL and M. L. G. VAN GASSELT, "Post-Dryout Heat Transfer in Steam Generator Tubes at High Pressures," *Int. J. Heat Mass Transfer*, **26**, *3*, 459 (1983); https://doi.org/10.1016/0017-9310(83)90050-9.
36. Y. KOIZUMI et al., "Post-Dryout Heat Transfer of High Pressure Steam-Water Two-Phase Flow in Single Rod Channel and Multi Rod Bundle," *Nucl. Eng. Des.*, **99**, 157 (1987); https://doi.org/10.1016/0029-5493(87)90117-8.
37. W. M. ROHSENOW, "Post Dryout Heat Transfer Prediction Method," *Int. Commun. Heat Mass Transfer*, **15**, *4*, 559 (1988); https://doi.org/10.1016/0735-1933(88)90047-4.